


Article

Microemulsion-Assisted Synthesis of $\text{Ag}_2\text{CrO}_4@\text{MIL-125}(\text{Ti})-\text{NH}_2$ Z-Scheme Heterojunction for Visible-Light Photocatalytic Inactivation of Bacteria

Haoyu Yuan ^{1,2}, Chao Zhang ^{1,2}, Wenjing Chen ², Yuzhou Xia ², Lu Chen ², Renkun Huang ², Ruiru Si ³ and Ruowen Liang ^{1,2,*} 

¹ State Key Laboratory of Photocatalysis on Energy and Environment, Fuzhou University, Fuzhou 350002, China; yuanhaoyu4@163.com (H.Y.)

² Fujian Province University Key Laboratory of Green Energy and Environment Catalysis, Ningde Normal University, Ningde 352100, China

³ Fujian Key Laboratory of Agro-Products Quality and Safety, Fujian Academy of Agricultural Sciences, Fuzhou 350003, China

* Correspondence: rwwliang@ndnu.edu.cn; Tel.: +86-591-8377-9362

Abstract: Metal-organic frameworks (MOFs) are new porous materials composed of metal centers and organic ligand bridges, which received great attention in the field of photocatalysis. In this work, $\text{Ag}_2\text{CrO}_4@\text{MIL-125}(\text{Ti})-\text{NH}_2$ (denoted as AgCr@M125) Z-scheme heterojunctions were synthesized via a simple microemulsion method, by which highly dispersed nano-sized Ag_2CrO_4 can be anchored uniformly on the surfaces of porous $\text{MIL-125}(\text{Ti})-\text{NH}_2$ (denoted as M125). Compared with pure M125 and Ag_2CrO_4 , the as-prepared AgCr@M125 hybrids show significant photocatalytic efficiency against inactivated *Staphylococcus aureus* (*S. aureus*), reaching over 97% inactivation of the bacteria after 15 min of visible light irradiation. Notably, the photocatalytic activity of the obtained 20% AgCr@M125 is about 1.75 times higher than that of AgCr-M125 , which was prepared via a traditional precipitation method. The enhanced photocatalytic antibacterial activity of the AgCr@M125 photocatalytic system is strongly ascribed to a direct Z-scheme mechanism, which can be carefully discussed based on energy band positions and time-dependent electron spin response (ESR) experiments. Our work highlights a simple way to enhance the antibacterial effect by coupling with Ag_2CrO_4 and M125 via a microemulsion-assisted strategy and affords an ideal example for developing MOFs-based Z-scheme photocatalysts with excellent photoactivity.

Keywords: $\text{MIL-125}(\text{Ti})-\text{NH}_2$; Ag_2CrO_4 ; *S. aureus*; Z-scheme; microemulsion method



Citation: Yuan, H.; Zhang, C.; Chen, W.; Xia, Y.; Chen, L.; Huang, R.; Si, R.; Liang, R. Microemulsion-Assisted Synthesis of $\text{Ag}_2\text{CrO}_4@\text{MIL-125}(\text{Ti})-\text{NH}_2$ Z-Scheme Heterojunction for Visible-Light Photocatalytic Inactivation of Bacteria. *Catalysts* **2023**, *13*, 817. <https://doi.org/10.3390/catal13050817>

Academic Editors: Kai Yang and Changlin Yu

Received: 10 March 2023

Revised: 19 April 2023

Accepted: 26 April 2023

Published: 28 April 2023



Copyright: © 2023 by the authors. Licensee MDPI, Basel, Switzerland. This article is an open access article distributed under the terms and conditions of the Creative Commons Attribution (CC BY) license (<https://creativecommons.org/licenses/by/4.0/>).

1. Introduction

With the rapid development of industrialization and the increase in population density year by year, bacterial pollution has become a major threat to human health [1]. Traditional disinfection methods, such as chemical disinfection, thermal radiation, and physical disinfection are difficult to apply widely because they are environmentally unfriendly and expensive. Photocatalysis is considered a prospective and ecofriendly method for the elimination of harmful pollutants from wastewater, which has attracted widespread attention [2]. In the past decades, various materials, including inorganic metal oxides, metal sulfides, and organic semiconductors have been developed as photocatalysts. However, the available photocatalysts are still far from being efficient enough for actual applications. Therefore, exploring more high-performance photocatalysts to inactivate bacteria remains a great commercialization priority for photocatalysis [1–3].

Metal-organic frameworks (MOFs) are an emerging class of crystalline porous materials, formed by inorganic nodes and multifunctional organic linkers. Due to their fascinating characteristics, MOFs have been demonstrated to be outstanding photocatalysts. Particularly, Ti-based MOFs have raised much attention in the field of photocatalysis [4]. For

example, MIL-125(Ti)-NH₂ (simply labeled as M125) has a narrow band gap (2.6~2.8 eV) and exhibits significant photo availability to initiate chemical photocatalytic reactions. Fu et al. first investigated MIL-125(Ti)-NH₂ to facilitate the photoreduction of carbon dioxide under visible light illumination by using triethanolamine as an electron donor [4]. However, the shortage of active sites and the weak separation resolution of photoinduced vectors decrease the photocatalytic performance of neat MOFs. To further enhance their photoactivity, many strategies have been proposed, such as ligand functionalization, dye sensitization, carbon material decoration, and metal decoration [5]. Incorporating the second semiconductor to construct binary MOFs-based heterostructures [5,6] is supposed to be a superior method to improve the optical properties and boost the charge separation efficiency of MOFs photocatalysts. Z-scheme heterojunction structure is an advanced charge transport mechanism, which retains the valence band (VB) and conduction band (CB) [6] at their highest potential levels in the composite. Interestingly, coupling two semiconductors capable of matching band-edge positions to construct an artificial Z-scheme photocatalytic system is an efficient and controllable method for improving photocatalytic performance that promotes spatial separation of photogenerated carriers while retaining excellent redox capabilities [7].

Choosing the stable and band structure and matching the second component semiconductor are crucial for achieving hierarchically Z-scheme heterojunction. Ag₂CrO₄ has caught the attention of researchers in recent decades due to its narrow band gap (~1.75 eV) and high photocatalytic activity [8]. In addition, its unique crystalline structure of large O-Ag-O angle and long O-Ag chemical bond makes the charge transfer easier. It is well known that structure determines performance, and the activity of photocatalysts is usually limited by their structure and morphology, which is largely controlled by the synthesis method [9]. When using traditional precipitation methods, it is easier to obtain relatively large size particles, which tend to agglomerate and exhibit uneven size distribution. Microemulsions, as an anisotropic and thermodynamically robust system, have been extensively used to make monodisperse, nanoscale particles with controlled morphology, which can shorten the diffusion process for photogenerated excitons and improve the utilization of light [9,10]. Although various MOFs-based Z-scheme heterojunction photocatalysts, such as FeO₃/g-C₃N₄ [11], C@HPW/CdS [12], and WO₃/BiOBr [13], have been reported for the past few years, there is rare research on the Ag₂CrO₄@MOFs composites and their photocatalytic disinfection performance [14–16].

Herein, we constructed Ag₂CrO₄@MIL-125(Ti)-NH₂ (simply labeled as AgCr@M125) composites in a convenient microemulsion-assisted way for the first time. The photocatalytic antibacterial (taking *S. aureus* as an example) was used as a probe reaction to explore the photocatalytic performance of AgCr@M125. The experimental results showed that the activity of the 20%AgCr@M125 was significantly increased, which could sterilize *S. aureus* within 15 min. The experimental results show that the reaction mechanism follows the Z-scheme model, which enables the material to have efficient photogenerated carrier separation and strong redox ability. This novel AgCr@M125 hybrids not only provide new insights for environmental remediation but also highlights a promising strategy to design more efficient Z-scheme photocatalysts.

2. Results and Discussion

2.1. Characterisations

As shown in Figure 1a, all the characteristic peaks of M125 are well consistent with previous reports [4,17]. Pristine Ag₂CrO₄ shows a high crystallinity and the characteristic peaks originated from its orthorhombic structure (JCPDS No. 26-0952). From the enlarged powder X-ray diffraction (XRD) pattern (Figure 1b), the XRD patterns of AgCr@M125 composites are similar to M125. At the same time, the crystalline peaks of (220), (031), (211), and (002) belonging to Ag₂CrO₄ can be detected, which can also prove the coexistence of Ag₂CrO₄ and M125 in these composites [18]. The intensity of the peaks corresponding to Ag₂CrO₄ in AgCr@M125 is quite faint, and it can be attributed to the low crystallinity or

small size of Ag_2CrO_4 particles. On the whole, the peak intensity of Ag_2CrO_4 gradually increases with the increase of Ag_2CrO_4 content [19].

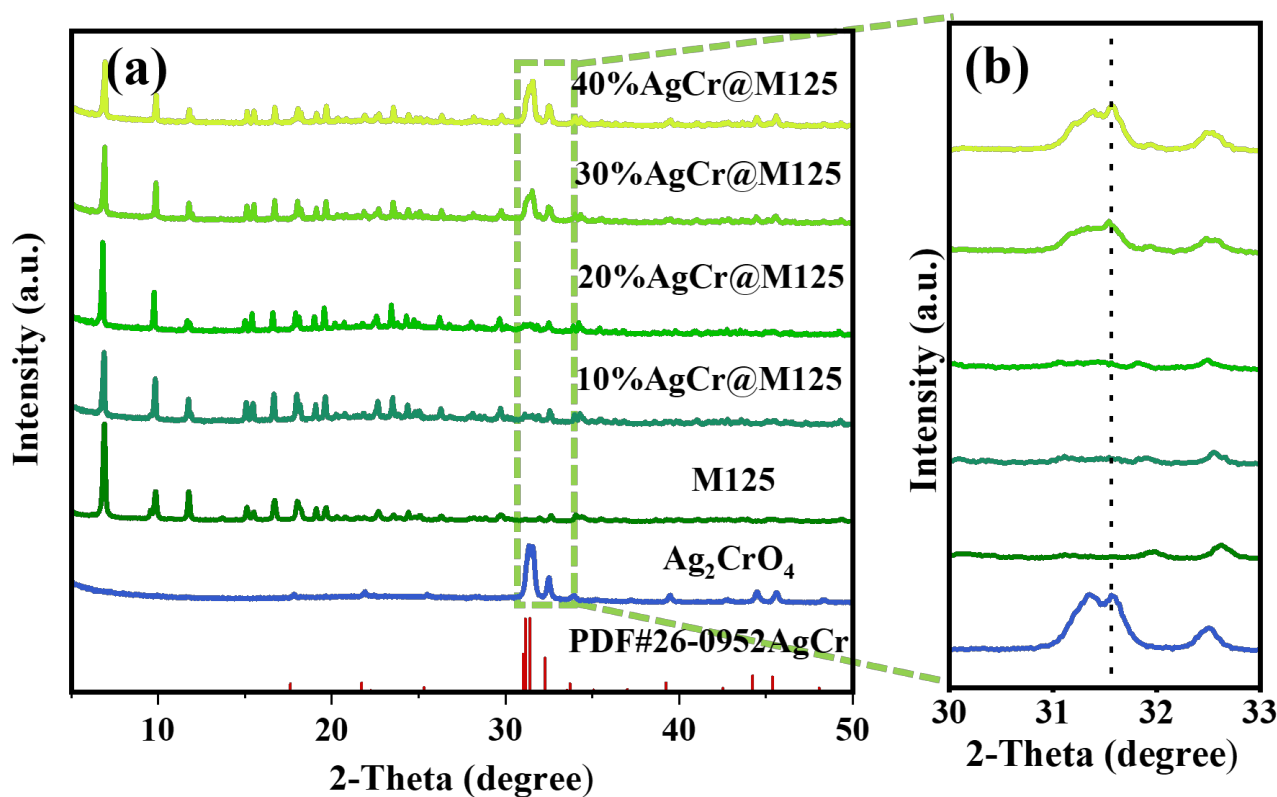


Figure 1. XRD patterns of (a) Ag_2CrO_4 , M125, and AgCr@M125 composites; (b) enlarged XRD patterns in the range of $30\text{--}33^\circ$.

The morphologies and microstructures of the samples were analyzed by scanning electron microscopy (SEM) and the results are illustrated in Figure 2. As shown in Figure 2a, the pure M125 shows a smooth pie-like structure with a diameter of about 500 nm (Figure 2a) [20]. The Ag_2CrO_4 particles prepared by the precipitation method show an irregular octahedral structure with a grain size of around 200 nm. In the case of the 20% AgCr@M125 , the smooth surfaces of the M125 are roughened after coating with the Ag_2CrO_4 , indicating that the tiny Ag_2CrO_4 particles uniformly distribute on the surface of M125. On the contrary, for the 20% AgCr-M125 , the Ag_2CrO_4 particles decorating the surface of M125 tend to aggregate, indicating the superiority of our microemulsion-assisted method. The microstructure of AgCr@M125 composites was further investigated and analyzed using transmission electron microscopy (TEM) and high-resolution TEM (HRTEM). As shown in Figure 2e,f, Ag_2CrO_4 nanoparticles with a diameter of about 10 nm are uniformly dispersed on the surface of M125 [21]. A set of lattice stripes can be seen in Figure 2g with a spacing of about 0.23 nm, corresponding to the (112) lattice spacing of the Ag_2CrO_4 orthorhombic phase [22,23]. It is of interest that the microemulsion-assisted growth of AgCr@M125 possesses a more uniform size compared with the conventional precipitation method. As for the 20% AgCr-M125 , the particle sizes of Ag_2CrO_4 particles are about 20–100 nm and become more severely agglomerated, which also coincides with the SEM results. In order to obtain a more visual confirmation of the atomic distribution, the TEM-mapping was performed. As illustrated in Figure 2m,n, AgCr@M125 prepared by the microemulsion method presents a symmetrical Ag elements distribution and uniform grain size, indicating a uniform distribution of Ag particles. On the other hand, for the AgCr-M125 , Ag elements are heavily agglomerated and the grain size varies greatly on the surface of AgCr-M125 .

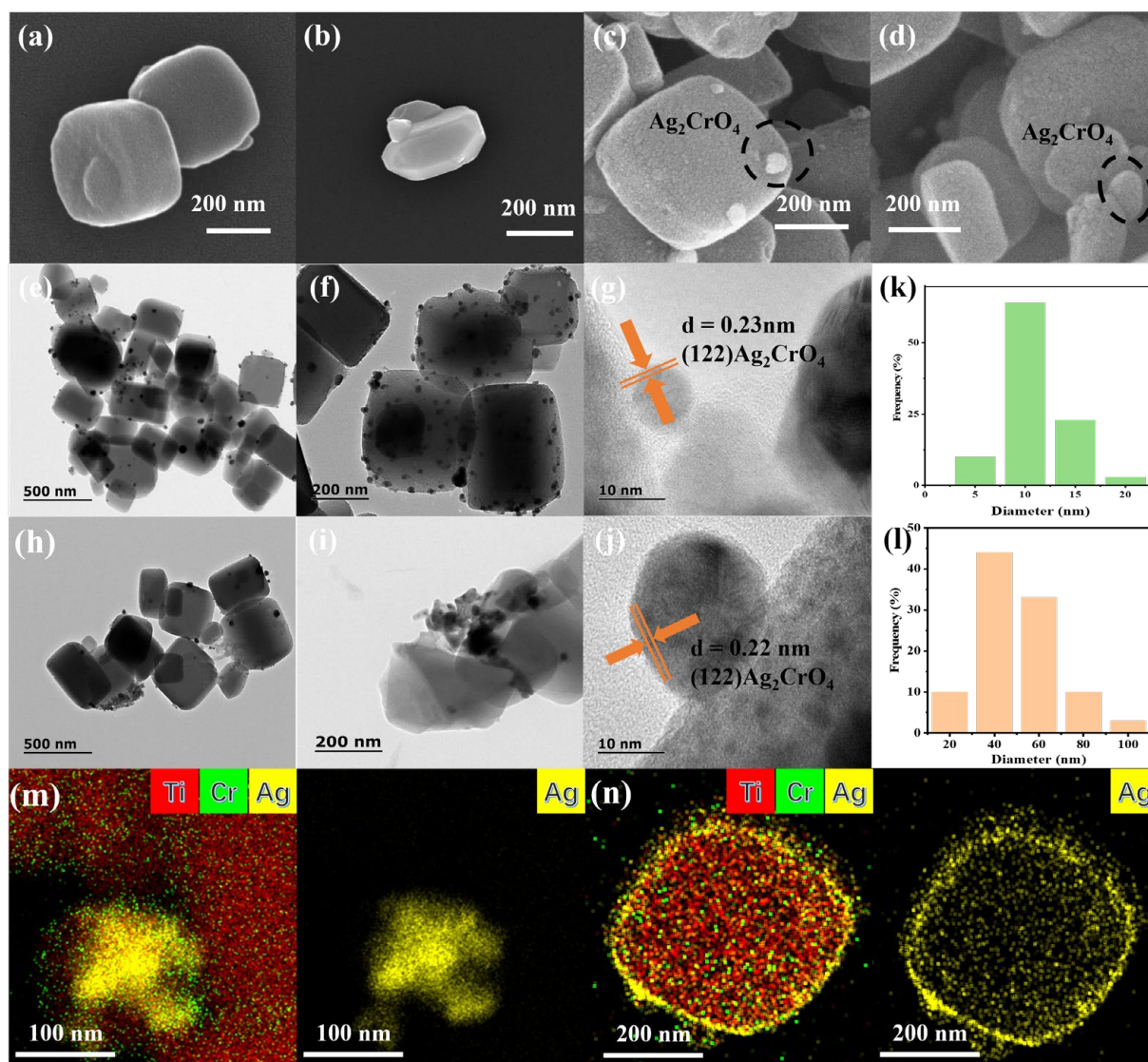


Figure 2. SEM images of (a) M125, (b) Ag₂CrO₄, (c) AgCr@M125, and (d) AgCr-M125; TEM images of (e–g) AgCr@M125 and (h–j) AgCr-M125; the corresponding size distribution of Ag₂CrO₄ particles (k) AgCr@M125 and (l) AgCr-M125; the mapping of (m) AgCr-M125 and (n) AgCr@M125.

The chemical structure was demonstrated by Fourier transform infrared (FTIR) spectroscopy. Figure 3a shows the FTIR spectra of the samples, where the characteristic peak at 3427 cm⁻¹ in the spectrum of M125 is the stretching of the surface hydroxyl group, and the peaks between 1380–1600 and 400–800 cm⁻¹ [24] are attributed to the stretching vibrational modes of the carboxylate and O–Ti–O, respectively. The FTIR spectra of AgCr@M125 are similar to that of M125 due to the absence of specific functional groups on the surface of Ag₂CrO₄, which also proves that the process of preparation using the microemulsion method did not destroy the structure of M125. Brunauer–Emmett–Teller (BET) surface areas of M125, Ag₂CrO₄, and AgCr@M125 samples were determined by adsorption–desorption measurements, and the results are displayed in Figure 3b. According to the BET classification, it can be observed that both M125 and AgCr@M125 adsorption–desorption belong to type IV isotherm [25], which indicates the mesoporous character of the samples. After Ag₂CrO₄ decorating, the specific surface area of AgCr@M125 decreased, illustrating the surface Ag₂CrO₄ loading partially blocked the original channel in M125.

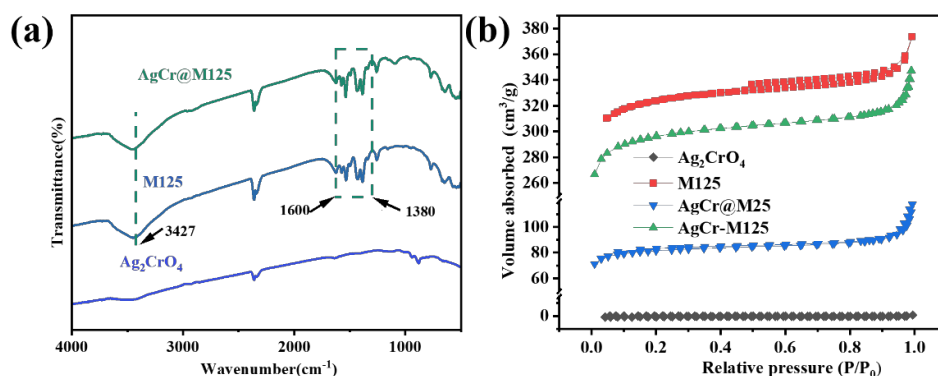


Figure 3. (a) FT-IR spectra of Ag_2CrO_4 , M125, and AgCr@M125; (b) N_2 adsorption–desorption isotherms for different catalysts.

The surface chemical compositions of AgCr@M125 composites were analyzed by X-ray photoelectron spectroscopy (XPS). The survey spectrum of AgCr@M125 shows that the synthesized composites contain five elements (Ti, C, O, N, and Ag) (Figure 4a). From Figure 4b, two characteristic peaks, 402.08 eV and 399.28 eV, are isolated from the high-resolution N 1s spectra. Compared to pure M125, two main peaks of Ti 2p_{1/2} and Ti 2p_{3/2} in the AgCr@M125 spectrum (464.48 eV and 458.68 eV) are pushed toward low binding energy (Figure 4c) [26]. In Figure 4d, a doublet Cr 2p peak of pure Ag_2CrO_4 at 576.08 eV (Cr 2p_{3/2}) and 585.89 eV (Cr 2p_{1/2}) is attributed to Cr⁶⁺, which is positively shifted for the AgCr@M125. Moreover, two peaks in the Ag 3d spectra of pure Ag_2CrO_4 can be distinguished at 367.5 and 373.5 eV, corresponding to the Ag 3d_{5/2} and Ag 3d_{3/2} of Ag⁺ (Figure 4e), respectively [27]. In the Ag 3d spectrum of the AgCr@M125 sample, these peaks are also positively shifted to 368.28 and 374.28 eV, respectively. A similar phenomenon has also been reported in Ag/MIL-125, $\text{Ag}_2\text{CrO}_4/\text{SCN}$, and $\text{Ag}_2\text{CrO}_4/\text{g-C}_3\text{N}_4$ composites [28–30]. Such transfer in binding energy suggests a robust interaction between Ag_2CrO_4 and M125 in AgCr@M125 rather than a simple physical mixing.

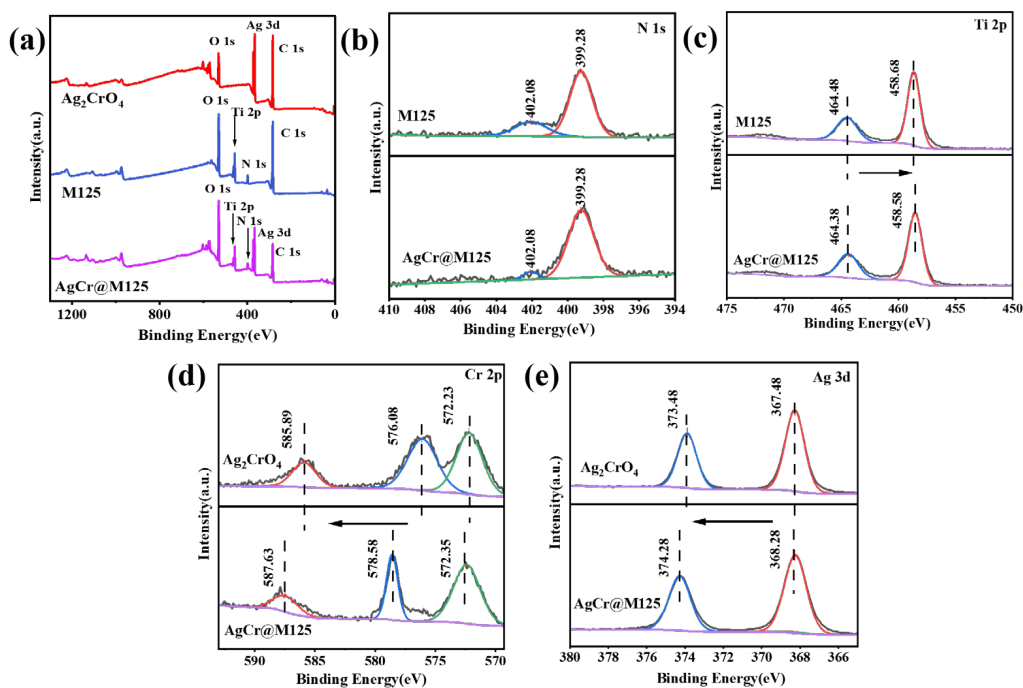


Figure 4. XPS spectra of M125, Ag_2CrO_4 , and AgCr@M125. (a) Survey scan; (b) N 1s high-resolution scan of (c) Ti 2p, (d) Cr 2p, and (e) Ag 3d.

2.2. Energy Band Structure

As can be seen in Figure 5a, the optical absorption edges of the original M125 and Ag_2CrO_4 are around 450 and 700 nm, respectively [28,31]. The light absorption capacity of the AgCr@M125 composites is higher than that of pure M125 and gradually increases with the increase of Ag_2CrO_4 content, meaning increased responsiveness to visible light. However, there is no significant change in the absorption edge of all composites, indicating Ag_2CrO_4 is not incorporated into the lattice of M125 and does not affect the structure of M125 itself. In addition, the band gap energies of all samples can be obtained by the following equation:

$$(\alpha h\nu)^n = A(h\nu - E_g) \quad (1)$$

where n is judged by the type of optical jump of the semiconductor (indirect ($n = 1/2$) or direct ($n = 2$)). According to Equation (1), the band gap energies of M125 and Ag_2CrO_4 are 2.75 eV and 1.87 eV, respectively (Figure 5b).

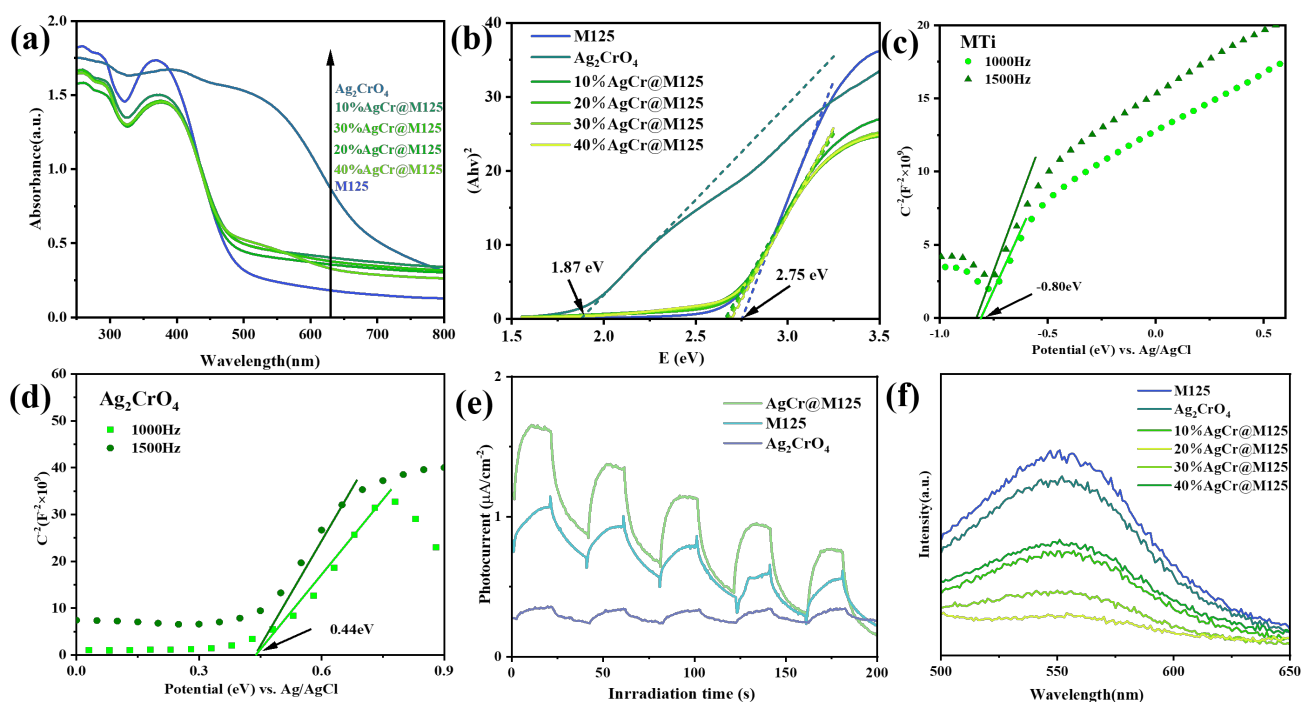


Figure 5. (a) UV-vis DRS spectra; (b) bandgap energy calculation of the as-obtained samples; Mott-Schottky plots of (c) Ag_2CrO_4 , (d) M125, (e) transient photocurrent, and (f) photoluminescence spectra of Ag_2CrO_4 , M125 and 20% AgCr@M125 .

To calculate the flat band potential (E_{fb}) of the original samples, Mott-Schottky (MS) plots were employed. The fact that the C^{-2} - E plot has a positive slope indicates that M125 and Ag_2CrO_4 both exhibit the typical behavior of n -type semiconductors. For M125 and Ag_2CrO_4 , the equivalent E_{fb} , or conduction band potential (E_{CB}), the values are -0.96 eV and $+0.36$ eV for Ag/AgCl at $\text{pH} = 6.8$, respectively. They are equivalent to -0.77 eV and -0.84 eV versus the typical hydrogen electrode ($\text{pH} = 6.8$). According to Equation (2):

$$E_{CB} = E_{VB} - E_g \quad (2)$$

The respective valence band potential (E_{VB}) for M125 and Ag_2CrO_4 are calculated as -0.6 eV and 0.64 eV, respectively. The photogenerated carrier separation capability of AgCr@M125 was evaluated by the photocurrent response [29–32]. As shown in Figure 5e, the photocurrent intensity of AgCr@M125 is significantly higher than that of the original M125 and Ag_2CrO_4 , which means that this composite can separate and transfer photogenerated carriers more efficiently. As the separation of photogenerated electron-hole

pairs is another critical factor affecting photocatalytic activity, the photogenerated carrier's separation efficiency is demonstrated by photoluminescence spectroscopy. As can be seen from Figure 5f, the peak intensity of 20%AgCr@M125 is lower than those of the pure substances, implying the lowest recombination rate of photogenerated electron–hole pairs for 20%AgCr@M125.

2.3. Antibacterial Activity

S. aureus photocatalytic disinfection was chosen as a model response to confirm the benefits of the AgCr@M125 hybrids [1,33]. The self-disinfection of *S. aureus* is essentially nonexistent in the absence of a photocatalyst, as shown in Figure 6a. After 15 min of visible light irradiation, the percentages of bacterial survival for individual M125 and Ag₂CrO₄ are 44.8% and 51.5%, respectively. Interestingly, all the AgCr@M125 hybrids show enhanced photocatalytic performances compared with the pristine M125, Ag₂CrO₄, and 20%AgCr–M125 under identical testing conditions. Only 55.6% of the bacteria can be destroyed by the 20%AgCr–M125, which is prepared by the precipitation method because Ag₂CrO₄ aggregates on the surface of M125 and due to the quick recombination of photogenerated electrons and holes. As shown in Figure 6c, the 20%AgCr@M125 sample shows the best antibacterial effect with <3% bacterial survival. Interestingly, when the content of Ag₂CrO₄ exceeds 20 wt%, it decreases the photocatalytic performance. As shown in Figure 6c, the disinfection efficiency against *S. aureus* decreased from 97.1% to 67.2%. This result is reasonable because, as the Ag₂CrO₄ content increases, it makes the Ag₂CrO₄ particles on the surface of M125 start to aggregate, while the excess Ag₂CrO₄ particles also shield the active sites on M125, which is consistent with the previous reports [34]. In comparison with other photocatalytic antibacterial studies, the 20%AgCr@M125 exhibits better or comparable activity for photocatalytic antibacterial activity under visible light irradiation (Table 1).

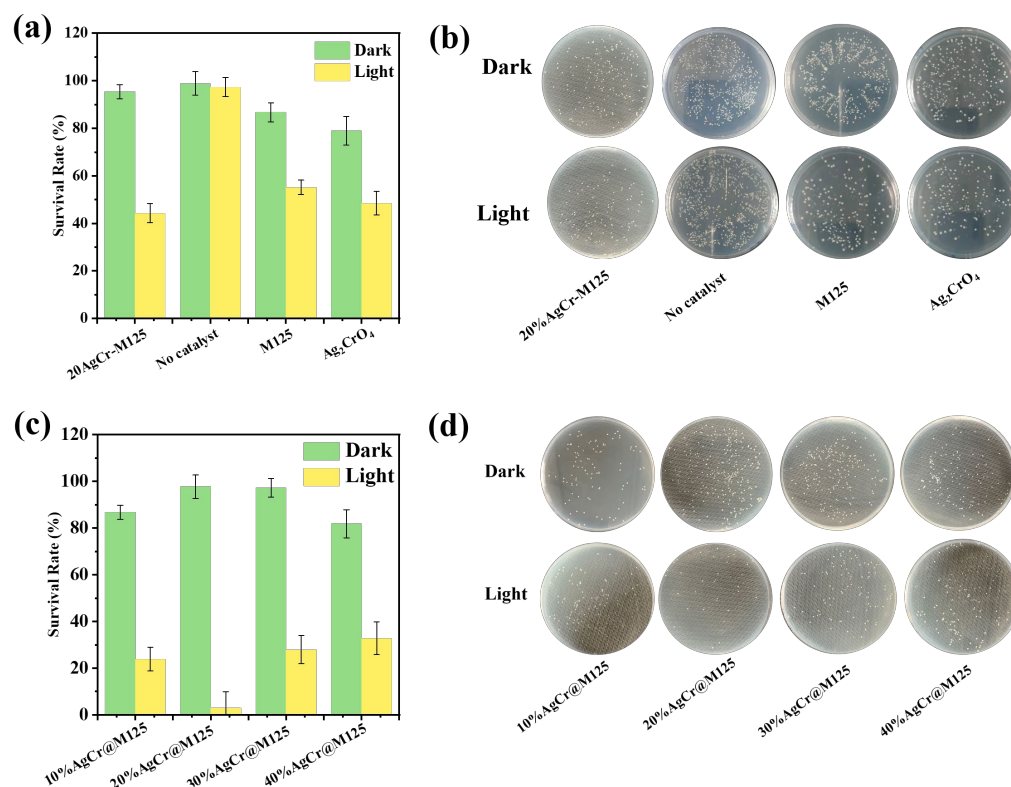
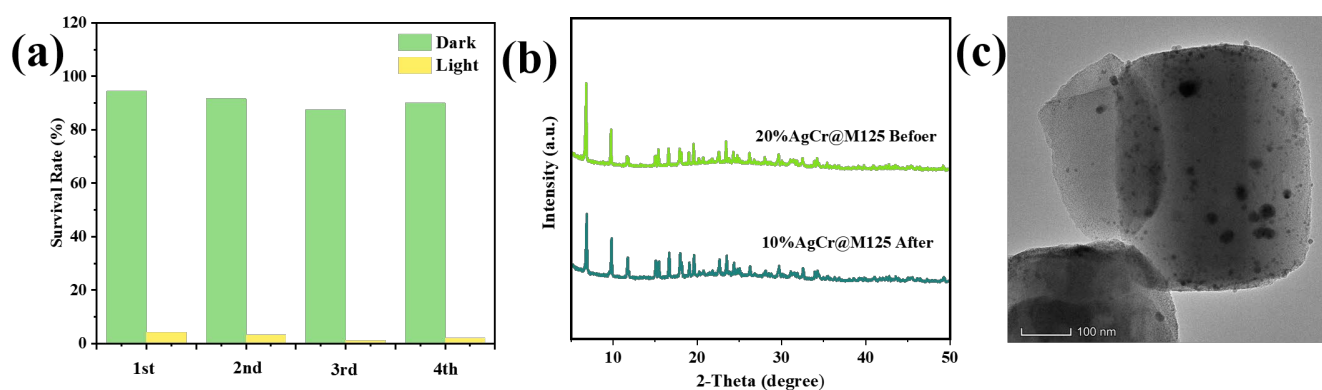


Figure 6. Antibacterial effect of AgCr@M125. (a,c): the survival rate of *S. aureus* after using different photocatalysts; (b,d): the colony plots of *S. aureus* after treatment with different photocatalysts.

Table 1. Comparison of the photocatalytic antibacterial (*S. aureus*) activities of 20%AgCr@M125 composites and other reported catalysts.

Photocatalyst	Dosage (g/L)	Irradiation Time (min)	Light Wavelength	Efficiency (%)	Ref.
20%AgCr@M125	0.2	15	300 W ($\lambda > 420$ nm)	97.7	This work
TiO ₂ -NH ₂ @Au NC	1.2	60	300 W ($\lambda > 400$ nm)	99.9	[35]
g-C ₃ N ₄ -V-TiO ₂	0.5	60	500W _{vis}	99.5	[36]
Ag ₂ S/NCs	0.1	60	NIR irradiation (808 nm)	97.3	[37]
ZnCl ₂ /TiO ₂ ,	4.0	120	270 W _{vis}	90.0	[38]
CQDs/g-C ₃ N ₄	1.0	220	300 W ($\lambda > 400$ nm)	99.9	[39]
BiVO ₄ -C300	1.0	120	300 W _{vis}	72.8	[40]
Mg/ZnO	2.0	180	300 W _{vis}	90.0	[41]
g-C ₃ N ₄ -AgBr	0.1	150	300 W _{vis}	99.9	[42]

Reusability and stability are important properties to examine the practicability of photocatalysts [43,44]. As shown in Figure 7a, the 20%AgCr@M125 exhibit a stable photocatalytic performance with no obvious activity of decaying after four cycles of photocatalytic reactions. The powder XRD patterns and TEM images confirm that the crystal structure and morphology of 20%AgCr@M125 are not destroyed after cycling experiments (Figure 7b,c), meaning that AgCr@M125 has good stability under visible light irradiation.

**Figure 7.** (a) Recyclability of 20%AgCr@M125 for the photocatalytic disinfection of *S. aureus* under visible light irradiation; (b) XRD patterns; (c) TEM image of 20% AgCr@M125 after the reaction.

2.4. Possible Photocatalytic Mechanism

To confirm the direct Z-scheme heterojunction mechanism, the electron spin resonance (ESR) technique was carried out under visible light. The generation of h^+ could be detected by 2,2,6,6-tetramethyl piperidinyl-1-aryloxy (TEMPO) because its radicals could be oxidized by h^+ . As shown in Figure 8a, the TEMPO characteristic peak decreases significantly with the extension of the light time, meaning that holes are photogenerated during the disinfection reaction. From Figure 8b,c, the radical signals of DMPO- \bullet OH and DMPO- \bullet O₂⁻ are not detected under dark conditions but appear when exposed to light. According to these findings, the major species involved in the photocatalytic reaction are h^+ , \bullet O₂⁻, and \bullet OH.

By a simple comparison of the H₂O/ \bullet OH and O₂/ \bullet O₂⁻ redox potentials versus the CB and VB potentials of M125 and Ag₂CrO₄. It can be found that \bullet OH radicals cannot form over pure M125, but can form over pure Ag₂CrO₄, as evidenced by the fact that the VB potential of Ag₂CrO₄ (2.51 eV vs. NHE) is more positive than that of E(\bullet OH/H₂O) (2.27 eV vs. NHE). On the contrary, \bullet O₂⁻ radicals cannot be generated over Ag₂CrO₄, but can be generated at the CB potential of M125 (-0.60 eV for NHE), which is more negative than E(O₂/O₂⁻) (-0.33 eV vs. NHE). If the electron-hole pair at the interface of AgCr@M125 follows the conventional type-II heterojunction mechanism, it is impossible to detect such a strong signal of \bullet OH and \bullet O₂⁻ radicals because the redox capacity of AgCr@M125

composites is impaired by such type-II structure [45–47]. Hence, we deduce that the charge transfer between Ag_2CrO_4 and M125 follows a Z-scheme heterojunction [45–50], and it not only promotes the effectiveness of photocatalytic disinfection but also benefits photogenerated carrier separation.

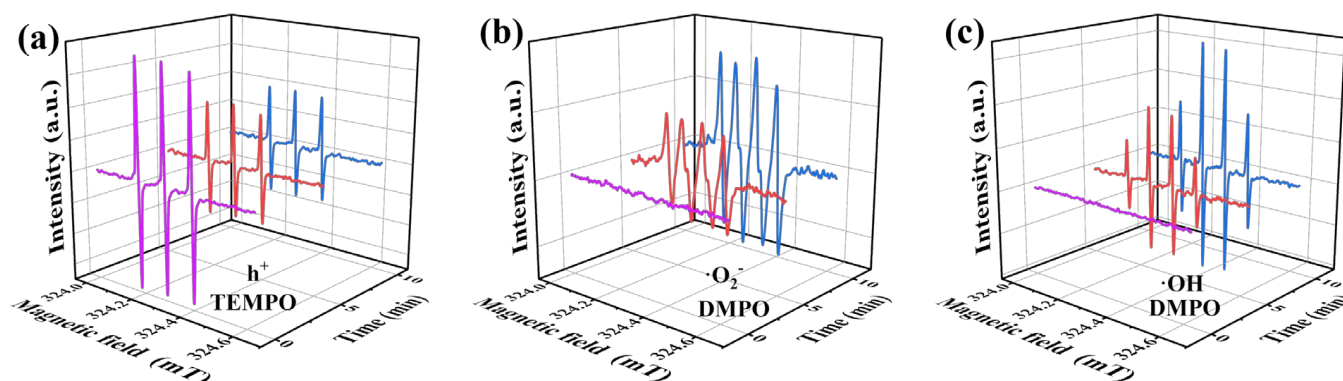
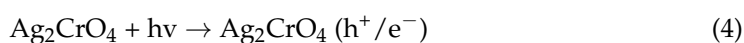
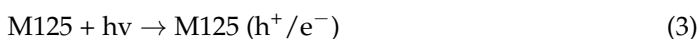


Figure 8. ESR spectra upon irradiation of AgCr@M125 heterostructure with different times: (a) h^+ , (b) $\bullet\text{O}_2^-$, and (c) $\bullet\text{OH}$.

A possible Z-scheme photocatalytic mechanism is schematically depicted in Figure 9. Under light irradiation, the electrons on the CB of Ag_2CrO_4 can easily transfer to the VB of M125 and recombined with the holes of M125 [48–51]. In this way, the photogenerated holes in M125 and the photogenerated electrons in Ag_2CrO_4 with poor redox ability can be sacrificed, and the electrons in M125 and the holes in Ag_2CrO_4 with strong redox ability remained and acted on the photocatalytic antibacterial. All the relevant reactions were described as follows [52,53]:



Photogenerated electrons at CB of M125 react with O_2 to produce $\bullet\text{O}_2^-$, which is a powerful oxidant in photocatalytic antibacterial. On the other hand, the holes in the VB of Ag_2CrO_4 can react with H_2O to generate $\bullet\text{OH}$ for favoring *S. aureus* oxidation. Therefore, $\bullet\text{OH}$, $\bullet\text{O}_2^-$, and the holes stored in the VB of Ag_2CrO_4 with strong oxidation ability could effectively kill the *S. aureus*. On the base of the above photocatalytic mechanism discussion, it can be suggested that the Z-scheme heterojunction mechanism can effectively separate photogenerated carriers and has a strong redox ability, thus improving the efficiency of photocatalytic antibacterial.

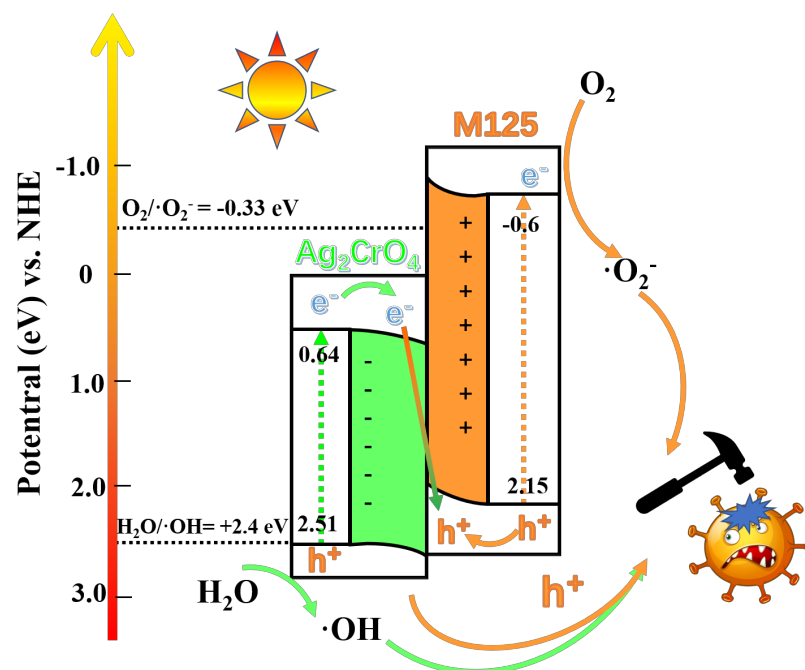


Figure 9. Reaction mechanism for photogenerated electron–hole pairs separation and transport over AgCr@M125 composite towards photocatalytic antibacterial.

3. Materials and Methods

3.1. Materials

All reagents and solvents were provided directly from commercial suppliers without further purification. The 2–amino–terephthalic acid (H_2ATA) was obtained from Alfa Aesar Chemical Co., Ltd. (Tianjin, China). Tetra butyl titanate and nutrient agar were obtained from Aladdin Reagent Co., Ltd. (Shanghai, China). Sodium chloride (NaCl), potassium dichromate (K_2CrO_4), silver nitrate (AgNO_3), cyclohexane, triton X–100, *n*–hexanol, *N,N*–dimethylformamide (DMF), anhydrous methanol, and anhydrous ethanol were supplied by Sinopharm Chemical Reagent Co., Ltd. (Beijing, China).

3.2. Catalyst Preparation

3.2.1. Preparation of M125

M125 (simply labeled as M125) was synthesized according to the literature with some modifications. In brief, 0.5 g of H_2ATA , 36 mL of DMF, and 4 mL of anhydrous methanol were added into a 100 mL Teflon–lined autoclave and stirred for 5 min. Subsequently, 1.2 mL of tetra butyl titanate was dripped into the above mixture and then stirred for 30 min. After heating with Teflon at 150 °C for 72 h, the product was left to cool at room temperature naturally. After that, the obtained M125 was collected by centrifuging and washing with DMF and anhydrous methanol several times to completely replace the guest DMF solvent molecule in the pores. Finally, the yellow powder sample was placed in a 70 °C oven for 12 h.

3.2.2. Preparation of AgCr@M125

A total of 16 mL of cyclohexane, 5.2 mL of triton X–100, and 3 mL of hexanol were mixed well at room temperature, followed by the slow addition of 100 mg of M125 and sonication for 30 min. After that, an amount of aqueous K_2CrO_4 (0.12 mol/L) was added drop by drop to the suspension to achieve a W/O reversed colloidal system, followed by rapid stirring for 1 h, to allow CrO_4^{2-} to be loaded on the surface of M125. Then, the same volume of AgNO_3 aqueous solution (0.24 mol/L) was added and continuously stirred for about 24 h. The precipitate was centrifuged and washed with ethanol and deionized water, and after drying at 70 °C for 24 h the final product was obtained. The theoretical mass

ratios of Ag_2CrO_4 were 0.1, 0.2, 0.3, and 0.4, and named 10%AgCr@M125, 20%AgCr@M125, 30%AgCr@M125, and 40%AgCr@M125, respectively. The pristine Ag_2CrO_4 was synthesized in a similar procedure but without the addition of M125.

3.2.3. Preparation of AgCr–M125

For comparison, AgCr–M125 was synthesized via a self-assembly method. Briefly, 100 mg of M125 was added into a known volume of K_2CrO_4 solution (0.12 mol/L) and ultrasonication was conducted for 30 min. Subsequently, an isometric AgNO_3 solution (0.24 mol/L) was added to this suspension and stirred for 24 h. The precipitate was centrifuged and washed with ethanol and deionized water, and after drying at 70 °C for 24 h the final products were obtained. The theoretical mass ratio of Ag_2CrO_4 was 0.2 and named 20%AgCr–M125.

3.3. Catalyst Preparation

Powder X-ray diffraction (XRD) was performed on a Bruker AXS D8 Advance X-ray diffractometer. The morphology of the sample was observed under a ZEISS Sigma 300 scanning electron microscope (SEM) and a US Thermo Fisher Talos F200S G2 transmission electron microscopy (TEM). Fourier transform infrared (FT-IR) spectra were recorded on a Thermo Scientific Nicolet iS10 infrared spectrophotometer. X-ray photoelectron spectroscopy (XPS) was observed on a US Thermo Scientific K-Alpha Science spectrometer. A Shimadzu UV-2700 equipment was used to collect UV-vis diffuse reflectance spectra (UV-vis DRS). The Edinburgh FLS1000 was used to collect photoluminescence spectra. On Micromeritics ASAP 2460 characteristics, the specific surface area of the samples was calculated. A JEOL JES-FA200 spectrometer was used to record electron spins (ESR). To capture the radical's signal, 5,5-dimethyl-1-pyrroline-N-oxide (DMPO) and 2,2,6,6-tetramethyl-1-piperidinyloxy (TEMPO) were used.

Based on a standard three-electrode cell system, electrochemical measurements were carried out, utilizing a Pt plate and Ag/AgCl electrode as the counter and reference electrode, respectively. The electrolyte was a 0.2 M Na_2SO_4 solution aqueous (pH = 7). After sonicating in ethanol for 30 min and drying at 353 K, the working electrode was cleaned using fluorine-doped tin oxide (FTO) glass. To create a slurry for the experiment, 5 mg of the sample was sonicated in 0.5 mL of DMF to ensure uniform sample dispersion. To improve adhesion, the pretreatment FTO glass was evenly covered with a coating of slurry and further dried at 393 K. After that, the scotch tape was removed and the uncoated part of the electrode was isolated with epoxy resin, leaving a 0.25 cm² exposed area to modify the sample. Bias-free photocurrent measurements were taken on a BAS Epsilon workstation, and a CHI0E A5225 workstation was used for Mott–Schottky texts.

3.4. Assessment of Antibacterial Activity

The photocatalytic antibacterial effect was evaluated using *S. aureus* as a targeted contaminant. A concentration of 2×10^9 colony-forming units (CFU) mL⁻¹ of *S. aureus* was used for this study. The photocatalyst (10 mg) was dispersed in 40 mL of saline (0.9% NaCl (*w/v*)) and sterilized using an autoclave. A 300 W Xenon lamp (PLS-SXE300D, Beijing Perfect Light Source Technology Co., Ltd. (Beijing, China.)) with a 420 nm filter was used as the light source for the photocatalytic antibacterial experiments, and samples were taken one at a time with time intervals. The diluted solution (100 µL) was spread flat on an agar plate and incubated at 37 °C for 24 h to assess the inactivation performance by plate counting method.

4. Conclusions

In summary, AgCr@M125 nanocomposites were successfully synthesized by a facile microemulsion-assisted method. In this architecture, the highly dispersed Ag_2CrO_4 with a size of ~10 nm is evenly dispersed on the M125. Compared with the AgCr–M125 prepared by the precipitation method, the AgCr@M125 has more uniform Ag_2CrO_4 particle loading

and higher photocatalytic activity. The optimum composite with 20 wt.% Ag_2CrO_4 exhibits the best photocatalytic activity, and its *S. aureus* killing rate reaches 97% after 15 min of visible light irradiation. The enhancement in the photoactivity is attributed to the high dispersion of Ag_2CrO_4 particles and the Z-scheme heterojunction between Ag_2CrO_4 and M125, which provides an efficient transfer pathway for charge carriers while the composites with strong redox ability are endowed. Finally, a possible antimicrobial mechanism is proposed. This work expands the application of MOF materials and provides a good demonstration of the design of novel MOF-based Z-scheme photocatalysts.

Author Contributions: Conceptualization, H.Y. and R.L.; methodology, H.Y., R.L. and Y.X.; investigation, H.Y. and C.Z.; resources, H.Y., R.L., L.C. and Y.X.; data curation, H.Y. and W.C.; writing—original draft preparation, H.Y.; writing—review and editing, H.Y., R.L., R.H., R.S., L.C. and Y.X.; visualization, H.Y. and R.L.; supervision, R.L. and R.S.; project administration, R.H. and L.C.; funding acquisition, R.L. All authors have read and agreed to the published version of the manuscript.

Funding: This research was funded by the Scientific Research Fund Project of Ningde Normal University, grant number 2021ZDK06.

Data Availability Statement: The data presented in the study are available from the corresponding author.

Conflicts of Interest: The authors declare no conflict of interest.

References

1. Wang, S.; Xia, Y.; Yan, G.; Chen, M.; Wang, X.; Wu, L.; Liang, R. PDI bridged MIL-125(Ti)- NH_2 heterojunction with frustrated Lewis pairs: A promising photocatalyst for Cr(VI) reduction and antibacterial application. *Appl. Catal.* **2022**, *317*, 121798. [[CrossRef](#)]
2. Liu, S.; Jiang, X.; Waterhouse, G.I.N.; Zhang, Z.M.; Yu, L.M. Construction of Z-scheme Titanium-MOF/plasmonic silver nanoparticle/NiFe layered double hydroxide photocatalysts with enhanced dye and antibiotic degradation activity under visible light. *Sep. Purif. Technol.* **2021**, *278*, 119525. [[CrossRef](#)]
3. Li, T.; Li, Y.B.; Dai, X.C.; Huang, M.H.; He, Y.; Xiao, G.; Xiao, F.X. Ligand-triggered tunable charge transfer toward multifarious photoreduction catalysis. *J. Phys. Chem. C* **2019**, *123*, 4701–4714. [[CrossRef](#)]
4. Fu, Y.; Sun, D.; Chen, Y.; Huang, R.; Ding, Z.; Fu, X.; Li, Z. An amine-functionalized titanium metal-organic framework photocatalyst with visible-light-induced activity for CO_2 reduction. *Angew. Chem. Int. Ed. Engl.* **2012**, *51*, 3364–3367. [[CrossRef](#)] [[PubMed](#)]
5. Shang, Y.; Chen, X.; Liu, W.; Tan, P.; Chen, H.; Wu, L.; Ma, C.; Xiong, X.; Pan, J. Photocorrosion inhibition and high-efficiency photoactivity of porous $\text{g-C}_3\text{N}_4/\text{Ag}_2\text{CrO}_4$ composites by simple microemulsion-assisted co-precipitation method. *Appl. Catal.* **2017**, *204*, 78–88. [[CrossRef](#)]
6. Shi, S.; Han, X.; Liu, J.; Lan, X.; Feng, J.; Li, Y.; Zhang, W.; Wang, J. Photothermal-boosted effect of binary CuFe bimetallic magnetic MOF heterojunction for high-performance photo-Fenton degradation of organic pollutants. *Sci. Total Environ.* **2021**, *795*, 148883. [[CrossRef](#)]
7. Wang, S.M.; Wang, F.; Dong, Y.L.; Shivanna, M.; Dong, Q.; Mu, X.T.; Duan, J.; Yang, Q.; Zaworotko, M.J.; Yang, Q.Y. Reversed $\text{C}_2\text{H}_6/\text{C}_2\text{H}_4$ separation in interpenetrated diamondoid coordination networks with enhanced host-guest interaction. *Sep. Purif. Technol.* **2021**, *276*, 119385. [[CrossRef](#)]
8. Lu, C.; Wang, J.; Xu, F.; Wang, A.; Meng, D. Zn-doped SnO_2 hierarchical structures formed by a hydrothermal route with remarkably enhanced photocatalytic performance. *Ceram. Int.* **2018**, *44*, 15145–15152. [[CrossRef](#)]
9. Shi, L.; Liang, L.; Wang, F.; Liu, M.; Sun, J. Ag_2CrO_4 nanoparticles loaded on two-dimensional large surface area graphite-like carbon nitride sheets: Simple synthesis and excellent photocatalytic performance. *Dalton Trans.* **2016**, *45*, 5815–5824. [[CrossRef](#)] [[PubMed](#)]
10. Feng, S.; Tan, G.; Zhang, B.; Bi, Y.; Yang, Q.; Liu, T.; Liu, Y.; Wang, Z.; Wang, M.; Xia, A.; et al. Local surface plasmon resonance promotion of photogenerated electrons to hot electrons for enhancing photothermal CO_2 hydrogenation over $\text{Ni}(\text{OH})_2/\text{Ti}_3\text{C}_2$ catalysts. *Colloids Surf. A* **2023**, *661*, 130907. [[CrossRef](#)]
11. Habibi-Yangjeh, A.; Mousavi, M.; Nakata, K. Boosting visible-light photocatalytic performance of $\text{g-C}_3\text{N}_4/\text{Fe}_3\text{O}_4$ anchored with CoMoO_4 nanoparticles: Novel magnetically recoverable photocatalysts. *J. Photochem. Photobiol. A* **2019**, *368*, 120–136. [[CrossRef](#)]
12. Cui, Y.; Xing, Z.; Guo, M.; Qiu, Y.; Fang, B.; Li, Z.; Wang, Y.; Chen, P.; Zhou, W. Core-shell carbon colloid sphere@phosphotungstic acid/CdS as a Z-scheme heterojunction with synergistic adsorption, photothermal and photocatalytic performance. *Catal. Sci. Technol.* **2021**, *11*, 6080–6088. [[CrossRef](#)]
13. Liu, C.; Mao, S.; Wang, H.; Wu, Y.; Wang, F.; Xia, M.; Chen, Q. Peroxymonosulfate-assisted for facilitating photocatalytic degradation performance of 2D/2D WO_3/BiOBr S-scheme heterojunction. *Chem. Eng. J.* **2022**, *430*, 132806. [[CrossRef](#)]

14. Chen, C.; Xiao, G.; Zhong, F.; Dong, S.; Yang, Z.; Chen, C.; Wang, M.; Zou, R. Synergistic effect of carbon nanotubes bonded graphene oxide to enhance the flame retardant performance of waterborne intumescent epoxy coatings. *Prog. Org. Coat.* **2022**, *162*, 106598. [[CrossRef](#)]
15. Gao, D.; Zhang, Y.; Wu, K.; Min, H.; Wei, D.; Sun, J.; Yang, H.; Fan, H. One-step synthesis of ultrabright amphiphilic carbon dots for rapid and precise tracking lipid droplets dynamics in biosystems. *Biosens. Bioelectron.* **2022**, *200*, 113928. [[CrossRef](#)] [[PubMed](#)]
16. He, Z.; Liang, R.; Zhou, C.; Yan, G.; Wu, L. Carbon quantum dots (CQDs)/noble metal co-decorated MIL-53(Fe) as difunctional photocatalysts for the simultaneous removal of Cr(VI) and dyes. *Sep. Purif. Technol.* **2021**, *255*, 117725. [[CrossRef](#)]
17. Hu, Y.; Hu, X.; Xue, L.; Cui, B.; Du, Y. Preparation of CaCO₃ mediated BiOBr that rich (110) facet and research of the photocatalytic properties. *Appl. Surf. Sci.* **2022**, *598*, 153800. [[CrossRef](#)]
18. Khan, Z.A.; Goda, E.S.; Rehman, A.U.; Sohail, M. Selective antimicrobial and antibiofilm activity of metal-organic framework NH₂-MIL-125 against *Staphylococcus aureus*. *Mater. Sci. Eng. B* **2021**, *269*, 115146. [[CrossRef](#)]
19. Lan, Y.X.; Cho, Y.C.; Liu, W.R.; Wong, W.T.; Sun, C.F.; Yeh, J.M. Small-load rGO as partial replacement for the large amount of zinc dust in epoxy zinc-rich composites applied in heavy-duty anticorrosion coatings. *Prog. Org. Coat.* **2023**, *175*, 107332. [[CrossRef](#)]
20. Li, T.; Li, Y.; Wang, H.; Yu, J.; Xu, D.; Wang, H.G. Fe-Nx active sites embedded into metal-organic-framework-derived mesoporous carbon for highly efficient oxygen reduction. *J. Phys. Chem. Solids* **2023**, *176*, 111256. [[CrossRef](#)]
21. Li, W.; Chen, J.; Guo, R.; Wu, J.; Zhou, X.; Luo, J. Facile fabrication of a direct Z-scheme MoO₃/Ag₂CrO₄ composite photocatalyst with improved visible light photocatalytic performance. *J. Mater. Sci. Mater. Electron.* **2017**, *28*, 15967–15979. [[CrossRef](#)]
22. Li, Z.; Wang, X.; Wang, Z.; Wang, L.; Guo, Y.; Zhou, C.; Li, X.; Du, K.; Luo, Y. Nickel-cobalt layered double hydroxide nanosheets anchored to the inner wall of wood carbon tracheids by nitrogen-doped atoms for high-performance supercapacitors. *J. Colloid Interface Sci.* **2022**, *608*, 70–78. [[CrossRef](#)] [[PubMed](#)]
23. Liang, R.; He, Z.; Lu, Y.; Yan, G.; Wu, L. High-efficiency sandwich-like hierarchical AgBr-Ag@MIL-68(Fe) photocatalysts: Step-scheme photocatalytic mechanism for enhanced photoactivity. *Sep. Purif. Technol.* **2021**, *277*, 119442. [[CrossRef](#)]
24. Liang, R.; Huang, R.; Wang, X.; Ying, S.; Yan, G.; Wu, L. Functionalized MIL-68(In) for the photocatalytic treatment of Cr(VI)-containing simulation wastewater: Electronic effects of ligand substitution. *Appl. Surf. Sci.* **2019**, *464*, 396–403. [[CrossRef](#)]
25. Liang, R.; Wang, S.; Lu, Y.; Yan, G.; He, Z.; Xia, Y.; Liang, Z.; Wu, L. Assembling Ultrafine SnO₂ Nanoparticles on MIL-101(Cr) Octahedrons for Efficient Fuel Photocatalytic Denitrification. *Molecules* **2021**, *26*, 7566. [[CrossRef](#)]
26. Liang, R.; Yuan, H.; Wang, S.; Chen, F.; Si, R.; Wu, L.; Yan, G. Formation of CdS quantum dots on zeolitic imidazolate framework-67 dodecahedrons as S-scheme heterojunctions to enhance charge separation and antibacterial activity. *Sep. Purif. Technol.* **2022**, *303*, 122291. [[CrossRef](#)]
27. Hao, R.; Wang, G.; Jiang, C.; Tang, H.; Xu, Q. In situ hydrothermal synthesis of g-C₃N₄/TiO₂ heterojunction photocatalysts with high specific surface area for Rhodamine B degradation. *Appl. Surf. Sci.* **2017**, *411*, 400–410. [[CrossRef](#)]
28. Xu, D.; Cheng, B.; Wang, W.; Jiang, C.; Yu, J. Ag₂CrO₄/g-C₃N₄/graphene oxide ternary nanocomposite Z-scheme photocatalyst with enhanced CO₂ reduction activity. *Appl. Catal. B* **2018**, *231*, 368–380. [[CrossRef](#)]
29. Ouyang, Q.; Li, Z.; Liu, J. Synthesis of β-AgVO₃ nanowires decorated with Ag₂CrO₄, with improved visible light photocatalytic performance. *Semicond. Sci. Technol.* **2018**, *33*, 055010. [[CrossRef](#)]
30. Wu, S.X.; Gao, Z.C.; Li, L.Y.; Gao, W.J.; Huang, Y.Q.; Yang, J. High-efficient visible light photocatalytic degradation by nano-Ag-doped NH₂-MIL-125(Ti) composites. *Inorg. Chim. Acta* **2023**, *544*, 121233. [[CrossRef](#)]
31. Xu, D.; Cao, S.; Zhang, J.; Cheng, B.; Yu, J. Effects of the preparation method on the structure and the visible-light photocatalytic activity of Ag₂CrO₄. *Beilstein J. Nanotechnol.* **2014**, *5*, 658–666. [[CrossRef](#)] [[PubMed](#)]
32. Ren, J.; Wu, Y.; Dai, Y.; Sha, D.; Pan, J.; Chen, M.; Wang, J.; Wang, Q.; Ye, N.; Yan, X. Preparation and characterization of graphitic C₃N₄/Ag₃VO₄ with excellent photocatalytic performance under visible light irradiation. *J. Mater. Sci. Mater. Electron.* **2016**, *28*, 641–651. [[CrossRef](#)]
33. Yang, Y.; Yang, H.R.; Seo, H.; Kim, K.; Kim, J.H. Novel synthesis of porous Si-TiO₂ composite as a high-capacity anode material for Li secondary batteries. *J. Alloys Compd.* **2021**, *872*, 159640. [[CrossRef](#)]
34. Katsumata, H.; Molla, M.A.I.; Islam, J.B.; Tateishi, I.; Furukawa, M.; Kaneco, S. Dual Z-scheme heterojunction g-C₃N₄/Ag₃PO₄/AgBr photocatalyst with enhanced visible-light photocatalytic activity. *Ceram. Int.* **2022**, *48*, 21939–21946. [[CrossRef](#)]
35. Shanmugam, V.; Sanjeevamuthu, S.; Jeyaperumal, K.S.; Vairamuthu, R. Fabrication of heterostructured vanadium modified g-C₃N₄/TiO₂ hybrid photocatalyst for improved photocatalytic performance under visible light exposure and antibacterial activities. *J. Ind. Eng. Chem.* **2019**, *76*, 318–332. [[CrossRef](#)]
36. Xiong, K.; Li, J.; Tan, L.; Cui, Z.; Li, Z.; Wu, S.; Liang, Y.; Zhu, S.; Liu, X. Ag₂S decorated nanocubes with enhanced near-infrared photothermal and photodynamic properties for rapid sterilization. *Colloid Interface Sci. Commun.* **2019**, *33*, 100201. [[CrossRef](#)]
37. Xiao, G.; Zhang, X.; Zhang, W.; Zhang, S.; Su, H.; Tan, T. Visible-light-mediated synergistic photocatalytic antimicrobial effects and mechanism of Ag nanoparticles @chitosan-TiO₂ organic-inorganic composites for water disinfection. *Appl. Catal. B Environ.* **2015**, *170–171*, 255–262. [[CrossRef](#)]
38. Tang, C.; Liu, C.; Han, Y.; Guo, Q.; Ouyang, W.; Feng, H.; Wang, M.; Xu, F. Nontoxic carbon quantum dots/g-C₃N₄ for efficient photocatalytic inactivation of *Staphylococcus aureus* under visible light. *Adv. Healthc. Mater.* **2019**, *8*, 1801534. [[CrossRef](#)] [[PubMed](#)]
39. Deka, S.; Devi, M.B.; Khan, M.R.; Keerthana; Venimadhav, A.; Choudhury, B. Piezo-photocatalytic and photocatalytic bismuth vanadate nanorods with antibacterial property. *ACS Appl. Nano Mater.* **2022**, *5*, 10724–10734. [[CrossRef](#)]

40. Iqbal, J.; Jan, T.; Ismail, M.; Ahmad, N.; Arif, A.; Khan, M.; Adil, M.; Haq, S.U.; Arshad, A. Influence of Mg doping level on morphology, optical, electrical properties and antibacterial activity of ZnO nanostructures. *Ceram. Int.* **2014**, *40*, 7487–7493. [[CrossRef](#)]
41. Deng, J.; Liang, J.; Li, M.; Tong, M. Enhanced visible–light–driven photocatalytic bacteria disinfection by g–C₃N₄–AgBr. *Colloids Surf. B* **2017**, *152*, 49–57. [[CrossRef](#)] [[PubMed](#)]
42. Molla, A.L.; Katsumata, H.; Furukawa, M.; Tateishi, I.; Kaneco, S. Synthesis of an iso–type graphitic carbon nitride heterojunction derived from oxamide and urea in molten salt for high–performance visible–light driven photocatalysis. *New J. Chem.* **2022**, *46*, 8999–9009. [[CrossRef](#)]
43. Shathy, R.A.; Fahim, S.A.; Sarker, M.; Quddus, S.; Moniruzzaman, M.; Masum, S.M.; Molla, M.A.I. Natural sunlight driven photocatalytic removal of toxic textile dyes in water using B–doped ZnO/TiO₂ nanocomposites. *Catalysts* **2022**, *12*, 308. [[CrossRef](#)]
44. Ye, L.; Wen, Z. ZnIn₂S₄ nanosheets decorating WO₃ nanorods core–shell hybrids for boosting visible–light photocatalysis hydrogen generation. *Int. J. Hydrogen Energy* **2019**, *44*, 3751–3759. [[CrossRef](#)]
45. Zhu, H.; Liu, N.; Wang, Z.; Xue, Q.; Wang, Q.; Wang, X.; Liu, Y.; Yin, Z.; Yuan, X. Marrying luminescent Au nanoclusters to TiO₂ for visible–light–driven antibacterial application. *Nanoscale* **2021**, *13*, 18996–19003. [[CrossRef](#)]
46. Abulizi, A.; Zhou, L.; Kadeer, K.; Tursun, Y.; Talifu, D. Photo–ultrasonic assisted in–situ synthesis of RGO/Ag₂CrO₄ photocatalyst with high photocatalytic activity and stability under visible light. *Mater. Sci. Semicond. Process.* **2018**, *86*, 69–78. [[CrossRef](#)]
47. Zhang, N.; Zhang, Y.; Pan, X.; Yang, M.Q.; Xu, Y.J. Constructing ternary CdS–graphene–TiO₂ hybrids on the flatland of graphene oxide with enhanced visible–light photoactivity for selective transformation. *J. Phys. Chem. C* **2012**, *116*, 18023–18031. [[CrossRef](#)]
48. Zhang, P.; Shao, C.; Zhang, M.; Guo, Z.; Mu, J.; Zhang, Z.; Zhang, X.; Liu, Y. Bi₂MoO₆ ultrathin nanosheets on ZnTiO₃ nanofibers: A 3D open hierarchical heterostructures synergistic system with enhanced visible–light–driven photocatalytic activity. *J. Hazard. Mater.* **2012**, *217*, 422–428. [[CrossRef](#)]
49. Zou, J.; Mao, D.; Wee, A.T.S.; Jiang, J. Micro/nano–structured ultrathin g–C₃N₄/Ag nanoparticle hybrids as efficient electrochemical biosensors for l–tyrosine. *Appl. Surf. Sci.* **2019**, *467*, 608–618. [[CrossRef](#)]
50. Feng, H.; Zhang, C.; Luo, M.; Hu, Y.; Dong, Z.; Xue, S.; Chu, P.K. A dual S–scheme TiO₂@In₂Se₃@Ag₃PO₄ heterojunction for efficient photocatalytic CO₂ reduction. *Nanoscale* **2022**, *14*, 16303–16313. [[CrossRef](#)]
51. Liu, X.; Chen, C.; Chen, P.; Wang, L. Ultrafast degradation of SMX and TC by CoSiO_x activated peroxy mono sulfate: Efficiency and mechanism. *RSC Adv.* **2023**, *13*, 3103–3111. [[CrossRef](#)] [[PubMed](#)]
52. Liu, Z.; Jiang, Y.; Liu, X.; Zeng, G.; Shao, B.; Liu, Y.; Liu, Y.; Zhang, W.; Yan, M.; He, X. Silver chromate modified sulfur doped graphitic carbon nitride microrod composites with enhanced visible–light photoactivity towards organic pollutants degradation. *Compos. Part B* **2019**, *173*, 106918. [[CrossRef](#)]
53. Zhang, G.; Yuan, X.; Xie, B.; Meng, Y.; Ni, Z.; Xia, S. Svacancies act as a bridge to promote electron injection from Z–scheme heterojunction to nitrogen molecule for photocatalytic ammonia synthesis. *Chem. Eng. J.* **2022**, *433*, 133670. [[CrossRef](#)]

Disclaimer/Publisher’s Note: The statements, opinions and data contained in all publications are solely those of the individual author(s) and contributor(s) and not of MDPI and/or the editor(s). MDPI and/or the editor(s) disclaim responsibility for any injury to people or property resulting from any ideas, methods, instructions or products referred to in the content.